ARTICLE

Emergence and full 3D-imaging of nodal boundary Seifert surfaces in 4D topological matter

Linhu Li[1]*, Ching Hua Lee[1,2]* & Jiangbin Gong [1]*

The topological classification of nodal links and knot has enamored physicists and mathematicians alike, both for its mathematical elegance and implications on optical and transport phenomena. Central to this pursuit is the Seifert surface bounding the link/knot, which has for long remained a mathematical abstraction. Here we propose an experimentally realistic setup where Seifert surfaces emerge as boundary states of 4D topological systems constructed by stacking 3D nodal line systems along a 4th quasimomentum. We provide an explicit realization with 4D circuit lattices, which are freed from symmetry constraints and are readily tunable due to the dimension and distance agnostic nature of circuit connections. Importantly, their Seifert surfaces can be imaged in 3D via their pronounced impedance peaks, and are directly related to knot invariants like the Alexander polynomial and knot Signature. This work thus unleashes the great potential of Seifert surfaces as sophisticated yet accessible tools in exotic bandstructure studies.

[1] Department of Physics, National University of Singapore, Singapore 117551, Republic of Singapore. [2] Institute of High Performance Computing, A*STAR, Singapore 138632, Singapore. *email: phylli@nus.edu.sg; calvin-lee@ihpc.a-star.edu.sg; phygj@nus.edu.sg

The irresistible allure of topological physics has brought together generations of physicists and engineers in witnessing how abstract beauty and experimental pragmatism coincide. In higher dimensions especially, the language of topology enables the understanding of novel and unexpected phenomena in terms of universal and robust motifs. A quintessential example is given by nodal knots existing in momentum space, where the knotted structure leads to new phases of matter protected by topological knot invariants. Unlike knotted molecules or optical vortices in real space[1-3], nodal knots consist of valence and conduction bands intersecting along one-dimensional (1D) lines in momentum space, which intertwine to form nodal loops (NLs) with rich knotted structures[4-13] with novel response properties[14], whose topological invariants take the form of polynomials rather than the $\mathbb{Z}_2$ or $\mathbb{Z}$ integers[11-13,15,16] of ordinary topological insulators[17,18]. Fundamental in constructing such invariants are the Seifert surfaces bounded by the nodal structure[15,16], which assume interesting, bubble-like shapes demarcating "drumhead" topological regions in the projected 2D surface Brillouin zone (BZ)[19-24].

As compact and orientable surfaces bounded by nodal knots or links, Seifert surfaces not only provide convenient visualization, but are also of core importance to topological classification. The linking properties of their homology generators can be used to compute[11,16] the Alexander polynomial—a classical knot invariant—of the NL or knot, hence distinguishing it from other nodal configurations. Indeed, Seifert surfaces are central to knot theory and low-dimensional topology[25], provoking many fascinating mathematical and computational problems, such as the uniqueness of a minimal genus Seifert surface[26], and their construction and visualization[27,28]. Its geometric appeal, e.g., appearing as a twisted band for the Hopf link, has also engendered much interest in other subfields, with alternative interpretations as contours of constant real space optical polarization azimuths[3], and dissipative bulk "Fermi" surfaces in non-Hermitian systems[29-34].

Despite their mathematical significance and appeal, Seifert surfaces do not naturally emerge from static 3D systems. To date, only their shadows (drumhead states) on the 2D surface BZ of a 3D topological matter has been connected with physical measurements[35-40]. On the other hand, recent advances in synthetic higher dimensional systems have lead to realizations of exotic topological matters, e.g., 4D quantum Hall systems[41-44]. Realizable as internal atomic levels[42], synthetic dimensions via periodic modulations[41,43,44], or genuinely new directions on a circuit lattice, the additional dimensions bring theoretical novelties[45,46] like 5D Weyl semimetals[47,48] close to physical reality. In particular, in RLC circuit setups lattice sites and positive/negative couplings between them are simulated by circuit nodes and capacitors/inductors respectively. Compared to existing higher dimensional optical systems with synthetic dimensions, circuit implementations have the advantages of being extremely versatile, inexpensive and reconfigurable[52-63] (see ref. [56] for a 3D Weyl circuit experiment), with nodes connected in any desired way free from constraints of locality or dimensionality.

Inspired by these developments, we propose to realize 3D NLs embedded in parent 4D nodal structures, such that Seifert surfaces naturally emerge as topologically robust zero-energy surfaces at their 3D boundaries. In essence, we propose to embed 3D NLs or their resultant knots in a 4D setup such that all desired NL structures are respectively associated with different quasimomentum values along the 4th dimension. Upon open boundary condition (OBC) taken along the 4th dimension, all such NL structures collapse onto the same 3D BZ and hence more complicated NL linkage or knots can be created. Having the 4th dimension makes the momentum space nodal topology much more experimentally accessible through Seifert surface imaging,

even in the face of added complexity. Unlike their 3D counterparts, 4D NL systems do not require any sublattice symmetry, and the 2D Seifert surfaces can be reconstructed more easily, compared with 1D NLs as thin structures detectable only at extremely high momentum-space resolution. More interestingly, arbitrarily many NLs can be systematically encapsulated in the 3D "boundary" BZ of a single 4D system with relatively simple coupling configurations. As we will demonstrate, such 4D systems are most suitably implemented via RLC circuit setups, where the extra 4th dimension is realized on equal footing as the other three spatial dimensions, and represents a "genuine" physical dimension in the sense that OBCs can be introduced to produce topological boundary modes. This, combined with the versatility in its implementation, is crucial in obtaining our topological boundary Seifert surfaces, which cannot exist in approaches where time takes the role of the 4th dimension[64].

Results

Drumhead states versus Seifert surfaces. We begin by clarifying the exact relationship between the 2D "drumhead" surface states of 3D nodal systems, and the 2D Seifert surface states within the 3D boundary of a 4D nodal system. Consider a minimal 2-band ansatz Hamiltonian

$$h(\mathbf{k}) = h_0(\mathbf{k})\mathbb{I} + \sum_{i=1}^{3} h_i(\mathbf{k})\sigma_i, \qquad (1)$$

with σ_i the i-th Pauli matrix acting in a pseudospin-1/2 space, $\mathbf{k}$ being the quasi-momentum vector. Nodes (pseudospin singularities) occur when $h_i(\mathbf{k}) = 0$ for all $i = 1, 2, 3$, such that the conduction and valence bands touch. In 3D, the nodes form NLs only when one of σ_i is constrained to be zero, typically by the combination of inversion and time-reversal (PT) symmetries of the system, i.e., $PTH^*(\mathbf{k})(PT)^{-1} = H(\mathbf{k})$ with PT a unitary operator, whose explicit form varies for different systems. But in 4D, NLs occur generically without any symmetry requirement, since the three constraints $h_i(\mathbf{k}) = 0$ still leave a nodal solution set with codimension 1. In this regard, 4D NL systems belong to the A class of the Altland-Zirnbauer classification[49-51], which ensures a $\mathbb{Z}$-type topology for even-dimensional gapped systems. Indeed, our 4D NL system can be comprehended as a 2D gapped system with two momenta taken as parameters, which possesses chiral boundary states protected by the same Chern topology as for a 2D quantum Hall system, as discussed in more details in the section "Nodal knot Seifert surface" and in Supplementary Note 1. At first glance, these 4D NLs do not seem interesting since nontrivial knots and links only exist in 3D, as any two 1D curves can pass by each other continuously through the 4th dimension and unravel the knot/link[15]. Yet, as we shall shortly show, the 3D boundary of such 4D nodal systems exhibits spectacular promise for the practical imaging of nodal knots.

Consider first the drumhead states in 3D nodal systems. Under OBCs, a typical 3D nodal system exhibits drumhead surface (2D boundary) states that fill the 2D region enclosed by the surface-projected NLs/knots (Fig. 1a, b), with dispersion given by $h_0(\mathbf{k})$. Essentially, drumhead states are boundary projections of a 2D surface stretched across the NLs in the 3D momentum space, i.e. a taut Seifert surface[15,16] of the NLs, with degeneracy corresponding to the multiplicity of the projection. But it has to be emphasized that the drumhead states, as a projection of the Seifert surface on a 2D plane, do not contain the original 3D geometric information, particularly of the knot over/under-crossing. While an alternative Seifert surface can be defined by the loci of equal pseudospin direction[3], it cannot be directly measured from the band structure. As such, the 2D boundary states are unable to encode complete information on the knotted
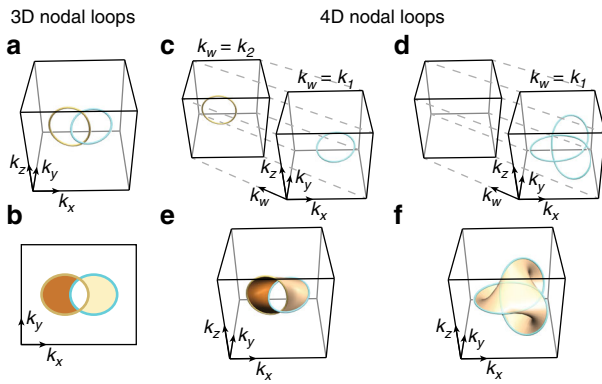
Fig. 1 3D and 4D nodal loops and their corresponding boundary states. **a** A Hopf-link in a 3D nodal loop (NL) system, and **b** the corresponding 2D boundary Brillouin zone (BZ) under open boundary conditions (OBCs) along z direction, with yellow and blue curves corresponding to projected NLs and brown shaded regions corresponding to topological boundary states. The Hopf-link in a 3D NL system gives rise to 2D topological drumhead states (dark and light brown) upon $\hat{z}$-boundary projection, retaining no information about the 3D over/under-crossings. **c** Two isolated NLs in a 4D system and **d** a Trefoil knot in a 4D system, with (**e**, **f**) their 3D boundary BZ under OBCs along $\hat{w}$ direction. Full information on the knot/link topology is retained in the Seifert surfaces [brown in (**e**-**f**)] arising from topological states in the 3D boundaries of 4D NL systems (**c**-**d**). A two-component boundary Hopf-link (**e**) can arise from a 4D NL system with two unlinked single loops (**c**) indexed by different $k_w = k_{1,2}$, while a one-component boundary Trefoil knot (**f**) and its Seifert surface also arises from a different 4D NL system (**d**). Here $k_{x,y,z,w}$ represent the quasi-momenta of 3D and 4D momentum spaces

nature of the nodal structure, which requires knowledge of its 3D configuration.

For physically realizing Seifert surfaces as boundary states and hence directly observing the knot topology, we consider 4D nodal systems defined in the three ordinary dimensions plus an additional dimension labeled by w. The key inspiration is that although the NLs are always unlinked and unknotted in 4D, they can be linked or knotted when "compressed" into 3D via (3D) boundary projection. This being the case, the topological boundary states of the given 4D topological matter, which interpolate the interior of the NLs, must necessarily form a Seifert surface embedded in a physical 3D BZ and terminating at NLs. This is illustrated in Fig. 1c, d and (e, f) with OBCs along the $\hat{w}$ direction. In Fig. 1c for instance, the 4D nodal structure is chosen to consist of two unlinked NLs embedded in their respective 3D BZ subspaces indexed by $k_w = k_{1,2}$, the quasi-momenta labeling their slice in the 4th dimension. With k_w projected out by OBCs, the two NLs become nontrivially linked in the 3D boundary BZ, and are interpolated by a Seifert Fermi (zero energy) surface (Fig. 1e). Similarly, a nodal Trefoil, which is unknotted in 4D [Fig. 1d], becomes knotted when projected into a 3D boundary (Fig. 1f). Alternatively, one may understand such 4D NL systems as 3D Weyl systems equipped with an additional dimension, such that Weyl points and their Fermi arcs trace out NLs and Seifert surfaces respectively along the additional dimension. With this insight, we can associate some exotic behaviors of Fermi arcs with the nontrivial topology of their parent NLs projected onto the 3D surface BZ, as discussed later when explicit constructions of nontrivial links and knots are introduced.

Before discussing general routes to topologically nontrivial Seifert surfaces as boundary states, we first explicitly describe the

simplest possible 4D Hamiltonian possessing a single NL:

$$
\begin{aligned}
h_{1\mathrm{NL}}(\mathbf{k}) = & (\cos k_x + \cos k_y + \cos k_z + \cos k_w - m)\sigma_a \\
& + (\sin k_w)\sigma_b + (\sin k_z)\sigma_c + h_0(\mathbf{k})\,\mathbb{I},
\end{aligned}
\tag{2}
$$

with x, y, z, w labeling the four dimensions, and $\sigma_a, \sigma_b, \sigma_c$ an arbitrary permutation of the three Pauli matrices. While the nodal structure is agnostic to the Pauli matrix basis, practical implementations may require specific choices dictated by symmetry. In this work, we assume no specific basis except when discussing the circuit realizations, where time-reversal symmetry holds. When $2 < m < 4$, Eq. (2) describes a single NL $\cos k_x + \cos k_y = m - 2$ in the $k_w = k_z = 0$ plane (Fig. 2a). Under $\hat{w}$-direction OBCs, topological boundary states must appear due to the bulk-edge correspondence associated with a nontrivial Chern number, as shown in the Supplementary Note 1 and Fig. 1. Those boundary states at zero energy then make up the Seifert surface $\cos k_x + \cos k_y < m - 2$, $k_z = 0$ matching the identified NL (blue).

Compared to 2D drumhead states in 3D NL systems, Seifert surface states of 4D NL systems are experimentally more robust as their existence does not require any symmetry of the system. They behave as chiral boundary states of 2D QH systems with two other momenta as system parameters (See Supplementary Fig. 1), and are thus immune to extra terms induced by noise or spatial modulations. Consider for instance a perturbation in $h_0(\mathbf{k})$. In 3D nodal systems, such terms will introduce momentum dependence in the energy and destroy the flatness of drumhead states and hence the boundary Fermi surface. However, in 4D nodal systems, they merely deform the boundary zero-energy surface in momentum space, which persist as 2D (zero-energy) Seifert surfaces of the NLs, thus being robust to the perturbation. Shown in Fig. 2b and c are two illustrative examples: $h_0(\mathbf{k}) \propto \cos k_y$ and $h_0(\mathbf{k}) \propto \sin k_y$. In the former case, the Fermi surfaces belonging to the two opposite OBC boundaries are fully separated and displaced in opposite directions, while in the latter they intersect along a line.

Nodal knot Seifert surfaces. We first show how a single nodal knot and its Seifert surface can be generically realized in the 3D boundaries of 4D NL systems. Starting from an ordinary NL system Hamiltonian defined in 3D,

$$
h_{3\mathrm{D}}(\mathbf{k}_{3\mathrm{D}}) = h_a(\mathbf{k}_{3\mathrm{D}})\sigma_a + h_b(\mathbf{k}_{3\mathrm{D}})\sigma_b,
\tag{3}
$$

we can always construct a 4D NL system Hamiltonian

$$
h_{4\mathrm{D}}(\mathbf{k}) = h_{3\mathrm{D}}(\mathbf{k}_{3\mathrm{D}}) + h_w(k_w),
\tag{4}
$$

$$
h_w(k_w) = t_w[(\cos k_w - 1)\sigma_a + (\sin k_w)\sigma_c],
\tag{5}
$$

with $\mathbf{k} = (\mathbf{k}_{3\mathrm{D}}, k_w) = (k_x, k_y, k_z, k_w)$ and t_w setting the scale of h_w. We shall offer two perspectives for understanding this resultant 4D system. From the first perspective, it may be understood as a series of identical 3D "unit blocks" arranged as a 1D chain along the $\hat{w}$ direction, with only nearest neighbor coupling between the blocks, such that each unit block is a 3D system $h_{3\mathrm{D}}(\mathbf{k}_{3\mathrm{D}})$ that contains the desired nodal knot (whose Seifert surface is yet to be revealed). Interestingly, $h_{3\mathrm{D}}$ and $h_{4\mathrm{D}}$ can be made to contain exactly the same bulk NLs. To see this, note that the gap of $h_{4\mathrm{D}}(\mathbf{k})$ closes when

$$
k_w = 0, \quad h_a^2(\mathbf{k}_{3\mathrm{D}}) + h_b^2(\mathbf{k}_{3\mathrm{D}}) = 0, \text{ or}
\tag{6}
$$

$$
k_w = \pi, \quad [h_a(\mathbf{k}_{3\mathrm{D}}) - 2t_w]^2 + h_b^2(\mathbf{k}_{3\mathrm{D}}) = 0.
\tag{7}
$$

By choosing $2t_w > \max[h_a(\mathbf{k}_{3\mathrm{D}})]$, Eq. 7 is never satisfied, and so
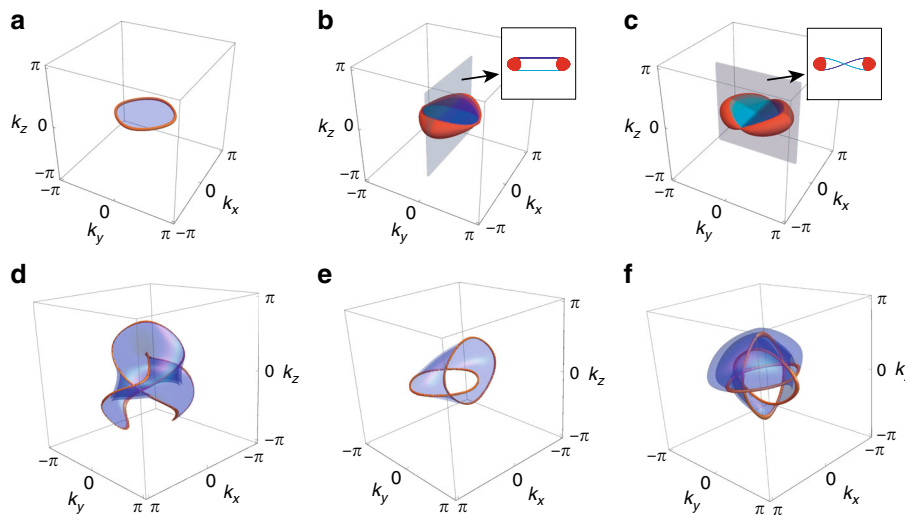
Fig. 2 Zero-energy states under open boundary conditions along the $\hat{w}$ direction for various 4D nodal loop systems. **a–c** Boundary states of a single 4D nodal loop of (Eq. (2)) with (**a**) and without (**b**, **c**) the perturbation term $h_0(\mathbf{k})\mathbb{I}$, with $\mathbb{I}$ the identity matrix acting on a pseudospin-1/2 space. The form of the perturbation is chosen to be $h_0(\mathbf{k}) = 0.4\cos k_y$ in (**b**), and $h_0(\mathbf{k}) = 0.4\sin k_y$ in (**c**), demonstrating the robustness of the Seifert surface against such perturbations. Red regions represent zero-energy bulk states (nodal solutions) whereas dark and light blue regions depict boundary states as Seifert surfaces of the nodal loops. Note that in (**c**), the light blue and dark blue regions are partially covered up by each other. **d** Boundary Trefoil knot and its Seifert surface states from Eq. (4). **e**, **f** Boundary Hopf-link and Borromean rings given by Eq. (8) and their Serfiet surfaces, with $N = 2$ and $N = 3$ linked loops respectively. $k_{x,y,z}$ represent the first three quasi-momenta of the boundary Brillouin zone with open boundary conditions along the fourth $\hat{w}$ direction

the gap closure conditions (Eqs. (6) and (7)) for $h_{4D}(\mathbf{k})$ reduce to that of $h_{3D}(\mathbf{k}_{3D})$.

To gain more insights, we shall introduce the second perspective, where we divide the four dimensions into two groups, namely, $(\hat{z}, \hat{w})$ and $(\hat{x}, \hat{y})$, such that $h_{4D}(\mathbf{k})$ can be viewed as a 2D system in $(\hat{z}, \hat{w})$ dimensions with k_x and k_y serving as two system parameters. Now if the bulk Hamiltonian $[h_a(\mathbf{k}_{3D}) + t_w(\cos k_w - 1)]\sigma_a + t_w(\sin k_w)\sigma_c + h_b(\mathbf{k}_{3D})\sigma_b$ features a nonzero topological Chern number, the chiral boundary states must emerge upon taking OBCs along the $\hat{w}$ direction, with the emergence of zero-energy boundary states requiring the obvious chiral-symmetry condition $h_b(\mathbf{k}_{3D}) = 0$. Moreover, the second condition $h_a(\mathbf{k}_{3D}) = 0$ represents the topological phase transition condition for such boundary states to appear (see Supplementary Note 1). All such zero-energy boundary states parameterized by (k_x, k_y) form a bona-fide Seifert surface (albeit not necessarily the minimal area Seifert surface) matching the nodal knot as the intersection of $h_a(\mathbf{k}_{3D}) = 0$ and $h_b(\mathbf{k}_{3D}) = 0$ surfaces. Illustrated in Fig. 2d is the boundary Seifert surface of a Trefoil knot with OBC along w direction, with its $h_{3D}(\mathbf{k}_{3D})$ and the designed $h_{4D}(\mathbf{k})$ detailed in Methods. The key takeaway of this construction is that, by connecting identical copies of 3D NL unit blocks with nearest neighbor couplings, one can realize not just the same NLs, but also their Seifert surfaces which contain the full topological information of the NLs. Such nearest neighbor couplings are easy to implement with circuits, as discussed later.

Seifert surfaces of arbitrarily many linked NL components. 4D extension can furthermore link arbitrarily many of such nodal structure components and their Seifert surfaces without increasing real-space complexity. Like illustrated in Fig. 1b, the 4th dimension allows multiple 3D NLs in different k_w subspaces to be embedded in the same 4D NL system. Given N different 3D NLs possessed by $h_{n,3D}(\mathbf{k}_{3D}) = h_{n,a}(\mathbf{k}_{3D})\sigma_a + h_{n,b}(\mathbf{k}_{3D})\sigma_b$, $n = 1, \ldots, N$, a 4D NL system that encapsulates them all can be

constructed as follows:

$$h_{N,4D}(\mathbf{k}) = \sum_{n=1}^{N} h_{n,3D}(\mathbf{k}_{3D})g_n(k_w) + f(k_w)\sigma_c. \quad (8)$$

Here $f(k_w) = 0$ at N values of k_w, i.e., $k_w = k_{w,n}$, with $n = 1, 2, \ldots, N$. Provided that each $g_m(k_w)$ at $k_w = k_{w,n}$ is nonzero when and only when $n = m$, the band touching condition for $h_{N,4D}(\mathbf{k})$ then yields a collection of all the N NLs we start with. Under OBCs in the $\hat{w}$-direction, all these NLs collapse into the same 3D boundary BZ, forming an intricately linked structure with N nodal components. As described in Methods with minimal and modular choices for $f(k_w)$ and $g_n(k_w)$, the topological boundary states of $h_{N,4D}$ consist of Seifert surfaces of N linked nodal structures.

Illustrated in Fig. 2e and f are two examples of Seifert surfaces with $N = 2$ and $N = 3$, corresponding to a Hopf-link and a set of Borromean rings respectively, with detailed Hamiltonians given in the Methods. The latter NL system has the curious property that each pair of loops is unlinked, even though the nodal structure has a nontrivial linkage characterized by the Milnor number[15]. Despite their intricacy, each NL in these systems is a simple unknot, realizable in simple 3D systems of $h_{n,3D}$ with only nearest neighbor couplings. Therefore, by taking unit cells along w direction as a 1D unit block, the 4D Hamiltonian of Eq. (8) for such systems describes a 3D block-lattice with only nearest neighbor couplings between these blocks along x, y, and z directions. The complexity is relegated to the interior structure within each unit block, yielding a relatively simple 3D block-lattice structure, as discussed in the following section of circuit realization.

Relation of Seifert surfaces to Fermi arcs. As discussed in the previous section and Supplementary Note 1, the NLs and the Seifert surface states originate from 2D Chern topology and exist without symmetry restrictions. Just like NLs in 3D which provide an analog to the parity anomaly of 2D Dirac semimetals[65], our
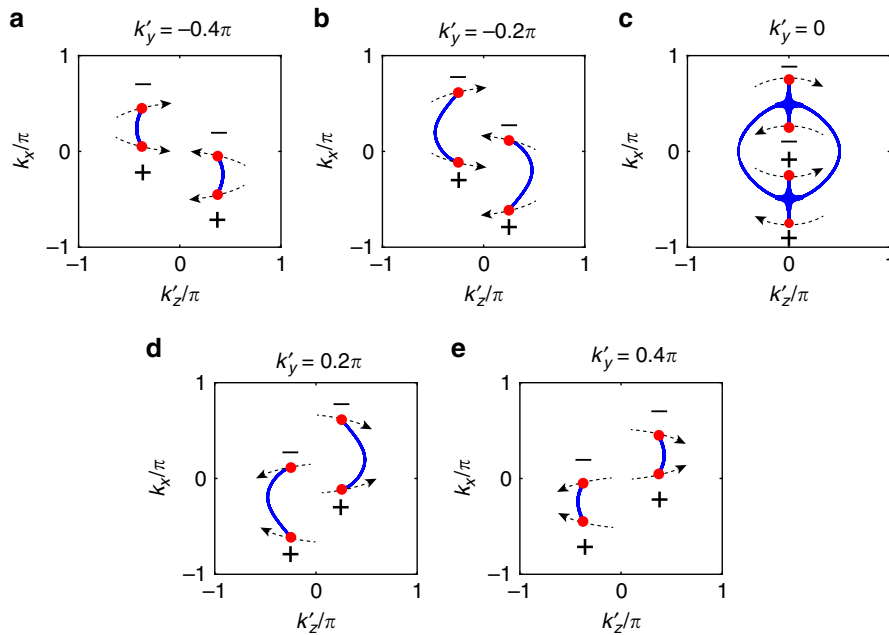
Fig. 3 Motion of Weyl points and Fermi arcs in an effective 3D model. A 4D nodal loop (NL) system can be viewed as an effective 3D nodal point system with an extra parameter. Each of (**a**–**e**) is a 2D "slice" of Fig. 2e, with $k'_y = k_y + k_z$, $k'_z = k_y - k_z$, and k'_y taken as a parameter describing the additional fourth dimension. Here $k_{x,y,z}$ represent the quasi-momenta of the 3D boundary Brillouin zone of a 4D system with open boundary conditions along $\hat{w}$ direction. The red points/blue lines correspond to the intersecting region of the nodal loops/Seifert surface states and the slices, analogous to the Weyl points/Fermi arcs in an effective 3D Weyl semimetal, with the two quasi-momenta of its 2D boundary Brillouin zone given by k_x and k'. The arrows show the movement of the Weyl points when increasing k'_y. The chirality of the Weyl points is shown by the plus or minus signs in the figure

systems can be viewed as 4D analogs of the 3D Weyl semimetals with chiral anomaly and Fermi arcs, equipped with the richer topological structures of knots and links. By introducing an additional fourth dimension to 3D Weyl systems, their Weyl points and Fermi arcs trace out the NLs and Seifert surfaces respectively along the fourth dimension. Therefore, we can associate some exotic behaviors of Fermi arcs with the nontrivial topology of their parent NLs projected onto the 3D surface BZ.

As illustrated in Fig. 3, the 4D Hopf-link Hamlitonian of Fig. 2e with $k'_y = k_y + k_z$, $k'_z = k_y - k_z$ has k'_y taken as a parameter describing the additional fourth dimension. With OBC along $\hat{w}$, the two Fermi arcs connecting Weyl points with opposite chiralities [defined in (k_x, k', k_w) space] can move in the 2D plane of k_x and k'_z, and exchange portions of their arcs by tuning k'_y from negative to positive, as demonstrated through Fig. 3a–e. Specifically, the Fermi arcs touch each other and form an exotic crossed flatband[66] at $k'_y = 0$ (Fig. 3c).

Imaging Seifert surfaces through circuit impedance measurements. Having described the mathematical construction of nodal Seifert surfaces, it is hence important to find an experimentally feasible realization of our approach. Below we discuss how a nontrivial link can be robustly realized and measured in an electrical circuit setup. Circuit realizations enjoy several advantages: (1) circuit connections are incredibly versatile, with coupling networks of arbitrarily non-locality or high dimensionality easily realizable with suitable wire configurations, (2) 3D boundary terminations are easily accessible as surface nodes of a circuit network and, perhaps most importantly, (3) massive Seifert Fermi surface degeneracies are easily detectable as pronounced "topolectrical" resonances already observed in other contexts[52–55,57–63], which we shall discuss in detail later in this section.

Unlike a quantum mechanical lattice governed by Schrödinger's equation, a circuit network is governed by Kirchhoff's equation. In a matrix form, Kirchhoff's law yields $I_\mu = \sum_\nu J_{\mu\nu} V_\nu$, where I_μ, V_μ are vectors with components representing the input current and electrical potential at node μ. The circuit Laplacian $J_{\mu\nu}$, which expresses the input currents in terms of the potentials, replaces the role of the Hamiltonian in determining the spectrum relevant to the impedance. In a standard RLC circuit at AC frequency ω, the resistors, inductors and capacitors respectively contribute off-diagonal terms $-R^{-1}$, $-(i\omega L)^{-1}$ and $-i\omega C$ to the Laplacian[54], consistent with the time-reversal symmetry condition

$$J^*(\mathbf{k}) = -J(-\mathbf{k}).$$

Since this mandates that any NLs must be symmetric in $\pm\mathbf{k}$, we shall frequently realize NLs in inverted-image pairs, such as those detailed in the Supplementary Note 2 and Fig. 2 for circuit realizations of unlinked nodal rings and a pair of Hopf-links.

Below we specialize to a 4D nodal circuit with minimally nontrivial boundary linkage, termed "2-link" below to distinguish from a Hopf link [Fig. 4]. Following Eq. (8), the circuit Laplacian is given by

$$J_{4D}(\mathbf{k}) = \left[h_{1,3D}(\mathbf{k}_{3D})(\cos k_w - 1) \right.$$
$$\left. + h_{2,3D}(\mathbf{k}_{3D})(\cos k_w + 1) + \sin k_w \sigma_3 \right] i\tau_2, \quad (9)$$

with σ_i and τ_i the Pauli matrices acting on two different pseudospin degrees of freedom, and

$$h_{1,3D}(\mathbf{k}_{3D}) = (\sin k_y)\sigma_1 + (m - \cos k_x - \cos k_y - \cos k_z)\sigma_2; \quad (10)$$
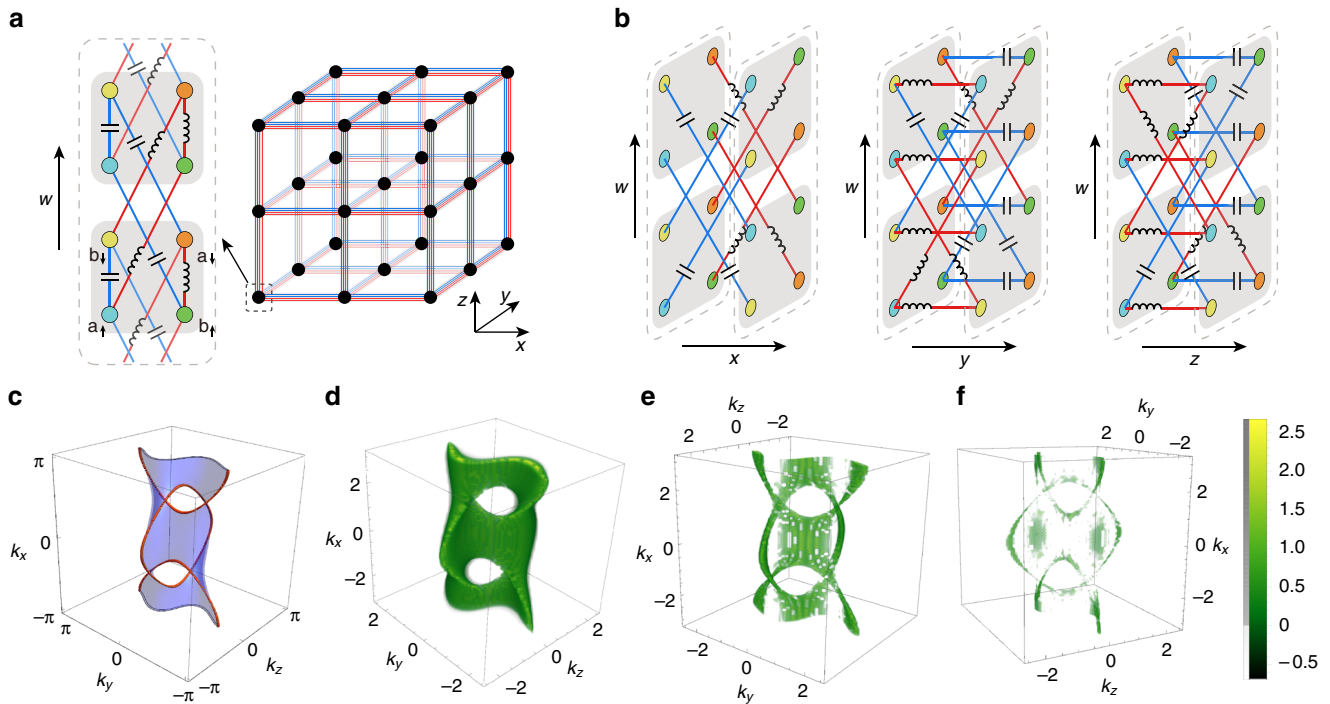
Fig. 4 2-link circuit and its topolectrical resonance simulations. **a** Sketch of our 2-link circuit (Eq. (9)) in terms of unit block internal structure (the dashed box) and overall connectivity. Gray shadows demarcate individual unit cells within a unit block, with each of the four sublattices colored differently, and red/blue lines indicating positive/negative couplings implemented by inductors/capacitors, as detailed in Methods. The open boundary (not shown) is normal to the w-direction. **b** Detailed illustrations of inter-unit-block circuit couplings along the x, y, and z directions. **c** Analytically computed nodal loops (NLs) (red loops) that bound a topologically robust Seifert surface (blue region) of the 2-link given by Eqs. (9), (10) and (11) with $m = 1.5$, which is accurately reconstructed from topolectrical resonance simulations via Eq. (13). Variation of impedances across intra-unit cell diagonal sublattices from the boundary to the bulk: [(**d**) $\log|Z_{11}(\mathbf{k}_{3D})|$, (**e**) $\log|Z_{22}(\mathbf{k}_{3D})|$, and (**f**) $\log|Z_{33}(\mathbf{k}_{3D})|$] were computed with realistic 1% disorder. From the 3D surface (**d**) towards its 4D bulk (**f**), the Seifert surface gradually decays into the bulk NLs. All simulations were performed with a $64 \times 64 \times 64$ boundary discretization

$$h_{2,3D}(\mathbf{k}_{3D}) = -(\sin k_z)\sigma_1 - (m + \cos k_x - \cos k_y - \cos k_z)\sigma_2. \tag{11}$$

Here $h_{1,3D}$ and $h_{2,3D}$ give mutually displaced NLs along the k_x-k_z and k_x-k_y planes respectively, and they are manifested in the 3D surface BZ of the 4D system, in the same manner of Fig. 1c and e. For each of $h_{1,3D}$ and $h_{2,3D}$, its NL is protected by $\sigma_1 h^*(\mathbf{k}_{3D})\sigma_1 = h(\mathbf{k}_{3D})$. Note that the tensor product with τ_2 acts on every term, thus does not affect the NL structure of the system. However, it is necessary to have it in our circuit construction for maintaining time-reversal symmetry. In terms of real-space lattice circuit connections, this construction corresponds to capacitive/inductive elements for positive/negative couplings respectively, as illustrated in Fig. 4a, b and detailed in Methods. In particular, Fig. 4a depicts a unit block with two unit cells in it and all the intral-unit-block hoppings, and Fig. 4b displays only the hoppings between different unit blocks. For $1 < m < 2$, the two loops are linked, as shown in Fig. 4c.

We now re-examine Kirchhoff's law in a general circuit context, and explain how the Seifert surfaces (extensive zero eigenvalues of the Laplacian) show up in impedance measurements. For a 4D circuit with OBCs in the $\hat{w}$ direction and PBCs in the other $\mathbf{k}_{3D}$ directions, Kirchhoff's law is expressed explicitly in terms of the boundary momentum $\mathbf{k}_{3D}$ as

$$I_a(\mathbf{k}_{3D}) = \sum_{b,\mathbf{k}'_{3D}} J_{ab}(\mathbf{k}_{3D}, \mathbf{k}'_{3D}) V_b(\mathbf{k}'_{3D}), \tag{12}$$

where components of $I_a(\mathbf{k}_{3D})$, $V_a(\mathbf{k}_{3D})$ represent the $\mathbf{k}_{3D}$-th intra-layer Fourier component of the input current and electrical

potential in layer a. Here the "layers" are 3D sublattices parallel to the open boundary along the w direction, which collectively make up the 4D circuit. Anticipating disorder (discussed further in the Supplementary note 3), we have not assumed that J_{ab} is diagonal in momentum (translation invariant).

The key reason why our Seifert surfaces are so easily detectable is that they represent extensive (scaling with a power of the system dimension) degeneracies which manifest as "topolectrical" resonances[54]. Consider a multi-terminal impedance measurement on a configuration with input currents $I_{b,r_1}, I_{b,r_2}, \ldots$ into nodes $(r_1, r_2, \cdots)$ at 3D layer b. We measure the potentials $V_{a,r_1}, V_{a,r_2}, \ldots$ at nodes of layer a, which is not necessarily the same as b. From Eq. (12), the potential and current Fourier components are related via

$$
\begin{aligned}
V_a(\mathbf{k}_{3D}) &= \sum_{b,\mathbf{k}'_{3D}} (J^{-1})_{ab}(\mathbf{k}_{3D}, \mathbf{k}'_{3D}) I_b(\mathbf{k}'_{3D}) \\
&\approx \sum_{n;b} \frac{\left[|\psi_n(\mathbf{k}_{3D})\rangle\langle\psi_n(\mathbf{k}_{3D})|\right]_{ab}}{j_n(\mathbf{k}_{3D})} I_b(\mathbf{k}_{3D}) \\
&= \sum_b Z_{ab}(\mathbf{k}_{3D}) I_b(\mathbf{k}_{3D})
\end{aligned}
\tag{13}
$$

with $Z_{ab}(\mathbf{k}_{3D})$ the $\mathbf{k}_{3D}$ intra-layer wavevector impedance, and j_n and $|\psi_n\rangle$ the n-th eigenvalue and eigenvector of the circuit Laplacian J, expressed in the $(a, \mathbf{k}_{3D})$ basis above. We have assumed negligible amounts of disorder in the circuit components, such that $\mathbf{k}_{3D} = \mathbf{k}'_{3D}$ on the second line. The crucial observation is that $V_a(\mathbf{k}_{3D})$ is expected to diverge when an extensive number of zero modes (with $j_n \approx 0$) are present. In

our context, the divergence of $V_a(\mathbf{k}_{3D})$ indicates a Seifert surface state at $\mathbf{k}_{3D}$ when a is the surface 3D layer; a similar though weaker divergence in the bulk will indicate a bulk nodal crossing at $\mathbf{k}_{3D}$.

To probe the Seifert surfaces, we simulate an experiment where currents enter nodes in unit cell layer $b = 1, 2$, or 3, layer 1 being the 3D boundary, with input current magnitudes modulated according to a chosen $\mathbf{k}_{3D}$ momentum wavevector. This is consistent with overall current conservation as long as $\mathbf{k}_{3D} \neq \mathbf{0}$. Next, we take the simulated voltage readings on nodes in layers $a = 1, 2$, and 3, and extract their $\mathbf{k}_{3D}$-th Fourier component. This procedure can be repeated for all $\mathbf{k}_{3D}$ momentum points in a discretized 3D boundary BZ, so as to map out regions of high resonance corresponding to the Seifert surfaces. The results for $\log|Z_{ab}(\mathbf{k}_{3D})|$ for the model of Eq. (9) is shown in Fig. 4d–f for 1% disorder [see the Supplementary Note 3].

As evident in Fig. 4c, d, we clearly observe a Seifert surface as pronounced resonance peaks at the boundary $(a, b) = (1, 1)$. These resonances gradually decay as the layer index under measurement moves towards the bulk (Figs. 4e, f), eventually morphing into the bulk NLs.

Topological classification through Seifert surfaces. Although the Seifert surface obtained is not the unique surface bounded by the NLs, valuable topological information of the bulk nodal knots, e.g. the Alexander polynomial[15], can nevertheless be extracted in
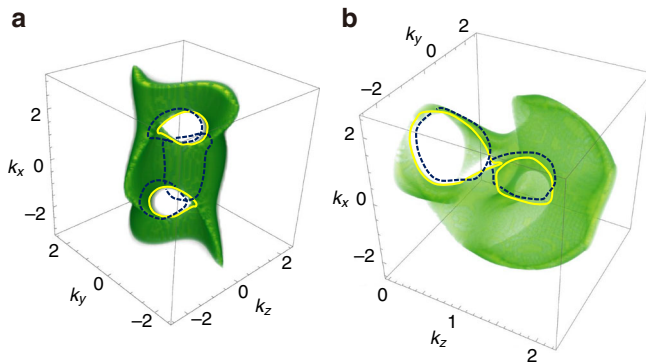

Fig. 5 Homology loops of the Seifert surfaces for different circuit NL systems. **a**, **b** The 2-link and trefoil nodal loop (NL) system reconstructed from topolectrical resonances, with the former corresponding to the system described by the Laplacian of Eq. (9), and the Laplacian of the latter explicitly given in Methods. The basis homology and lifted homology loops of their Seifert surfaces are given by the yellow and dashed blue curves respectively. The 2-link in (**a**) has $R = 3$ homology bases, and the trefoil knot in (**b**) has $R = 2$. Linking numbers between the yellow and dashed blue loops yield the Seifert matrix elements displayed in Table 1. For clarity, loops with vanishing linkages are omitted

a way independent of the explicit realization of the Seifert surface. This is the essence of the embedding-agnostic nature of topological invariants. Most obvious is the number of components (loops) N in the nodal structure, which corresponds to the number of punctures in the Seifert surface. Mathematically capping them with disks, the resultant Seifert surface becomes a closed Riemann surface with genus g handles. Although this genus is somewhat hard to directly visualize due to the intricate shape of the Seifert surface [see for instance Fig. 5, both with genus 1], it can be systematically computed by probing the connectivity of the the zero mode manifold as described below. The minimal g for a given NL structure is also a topological invariant.

More sophisticated invariants are encoded in the homology properties of the Seifert surface, as captured by the Seifert matrix S of linking numbers between its homology generators and those of its lifted (infinitesimally shifted) counterpart. The latter can be obtained by perturbing the coefficient of the system by a small real constant, which is easily implementable in circuits via a small AC frequency shift. Due to the robustness of the topology of the Seifert surface, we emphasize that the same Seifert matrix will be obtained regardless of the choice of the small frequency shift, as long as the same shift is consistently used in the measurements. For illustration, shown in Fig. 5a and b are the homology (yellow) and lifted homology (dashed blue) generators from topolectrical resonant Seifert surfaces, of 2-link (Fig. 4) and Trefoil knots respectively [see "Methods"].

In general, given any unknown nodal structure whose Seifert surface has been reconstructed, analogous homology loops can always be computed and their linking information put into a Seifert matrix of their linking numbers[15]. This matrix contains sufficient information for the topological characterization of the nodal structure. Firstly, the genus g of a Seifert surface with simply connected Seifert islands can be read from $g = (R + 1 - N)/2$, where N is the number of NL components and R is the number of homology basis generators (rank of the Seifert matrix). From them, NL knot invariants like the Alexander polynomial $A(t) = t^{-R/2} \mathrm{Det}\ (S - tS^T)$ and knot Signature (# positive - # negative eigenvalues of S) can be extracted (Table 1). For illustration, Table 1 shows the Seifert matrices extracted from simulation-reconstructed Seifert surfaces of a few common nodal structures, as well as the topological quantities computed from them. While two different realizations of the same nodal knot/ link can have different reconstructed Seifert surfaces and hence different Seifert matrices/genera, their resultant nodal topological invariants (Alexander polynomial and signature) always have to agree.

Discussion

In this work, the Seifert surface is elevated from a sophisticated but abstract mathematical concept to an experimentally accessible object crucial for topological characterization. We have devised

Table 1 Various Seifert surface properties and NL topological invariants

Link/Knot	N	Genus	Rank	Seifert matrix	A(t)	Signature
Hopf	2	0	1	-1	$\frac{t-1}{\sqrt{t}}$	-1
Trefoil	1	1	2	$\begin{pmatrix} -1 & 0 \\ 1 & -1 \end{pmatrix}$	$t + t^{-1} - 1$	-2
2-link	2	1	3	$\begin{pmatrix} -1 & 0 & 0 \\ 1 & 0 & -1 \\ 0 & 0 & 1 \end{pmatrix}$	0	0

Results are obtained from simulated boundary Seifert surface measurements of the nodal systems discussed. The combination of these topological invariants serves to precisely identify the nodal topology

an approach to realize rather arbitrary linkages and knot topologies in momentum-space NLs defined in an effective 4D space, but still implementable via practical experimental settings in 3D. Although our proposed circuits are thus fundamentally no more complex than existing 3D topological circuits[56], their more complicated connections between the unit blocks (see Fig. 4a, b) may require some additional care [See "Methods"]. That said, the additional topological robustness from extension to the 4th dimension should counteract the surmountable practical difficulties in circuit realizations.

The Seifert surfaces that can now be fully imaged encode full 3D nodal structure information of links and knots. In 3D NL systems, drumhead states have already been successfully imaged (e.g., in spin-orbit metal PbTaSe$_2$[35] and in phononic crystals[39]), but they only represent a projection of the Seifert surface on a 2D plane, and the full 3D nodal structure information can only be reconstructed by combining information about the drumhead states on surfaces oriented along different directions[11]. On the other hand, while bulk NLs can also be directly imaged in the 3D momentum space, they are 1D lines embedded in 3D, which requires relatively higher momentum-resolution, especially when the NLs consist of complex links or knots. As a comparison, our scheme realizes 2D Seifert surfaces embedded in the 3D surface BZ, which can be directly read out even with a lower resolution, and does not require information about different surfaces. With their existence rooted in 2D Chern topology, NLs/knots and their Seifert surface states are 4D analogs of 3D Weyl points and Fermi arcs. Yet, intricacies of their higher dimensional structure far transcend any characterization by a single Chern number. In the several explicit models discussed here and in the Supplementary Note 2, the lattice couplings are carefully designed to give clear and quantitative illustrations of the nontrivial NL topology through the topological invariants extracted from their topolectrically resonant Seifert surfaces. In this regard, RLC circuit setups are the most suitable experimental platform, as couplings can be simulated by independently tuned capacitors and inductors. Besides circuits, this work provides a potential scheme to realize exotic links and knots together with their Seifert surfaces in quantum systems, such as optical cold-atom lattices with one or more synthetic dimensions[67–70].

Methods

An explicit 4D model with a nodal Trefoil knot. In the main text, $h_{4D}(\mathbf{k})$ described by Eqs. (4) and (5) gives a 4D NL system with the desired nodal knot, and we have illustrated an example in Fig. 2d. The explicit model is given by Eqs. (4) and (5) with

$$h_a(\mathbf{k}_{3D}) = [\sin^3 k_z - 3\sin k_z \sin^2 k_x + \sin^2 k_y - (\cos k_z + \cos k_y + \cos k_x - m)^2],$$
(14)

$$h_b(\mathbf{k}_{3D}) = [-3\sin^2 k_z \sin k_x + \sin^3 k_x + 2\sin k_y(\cos k_z + \cos k_y + \cos k_x - m)],$$
(15)

with $t_w = 2$ and $m = 2$ yields the Trefoil knot model in Fig. 2(d). The above $h_{a,b}(\mathbf{k}_{3D})$ are obtained from

$$z^3 + w^2 = h_a(\mathbf{k}_{3D}) + i h_b(\mathbf{k}_{3D}),$$
(16)

with the regularized stereographic map

$$\begin{aligned} z &= \sin k_z - i \sin k_x, \\ w &= \sin k_y + i(\cos k_z + \cos k_y + \cos k_x - m). \end{aligned}$$
(17)

More general constructions of $h(\mathbf{k}_{3D})$ to obtain other nodal knots or links can obtained from various methods, e.g., the Hopf map indexed with a pair of numbers (p, q)[5]. For the Trefoil knot constructed above, $(p, q) = (3, 2)$.

Boundary states featuring arbitrarily many linked NLs. Equation (8) provides a scheme to realize 4D systems with arbitrarily many linked NLs in its 3D surface BZ, and here we provide an explicit ansatz to construct such 4D models, which we use

to construct the two examples in Fig. 2e, f. Consider the Hamiltonian

$$h_{N,4D}(\mathbf{k}) = \sum_{n=1}^{2M} h_{n,3D}(\mathbf{k}_{3D}) g_n(k_w) + f(k_w)\sigma_c,$$
(18)

where each individual $h_{n,3D}(\mathbf{k}_{3D})$ contains only two Pauli matrices $\sigma_{a,b}$ and may describe a 3D NL system. The conditions for this 4D Hamiltonian to display $2M$ NLs, each lying in a 3D slice with a different k_w properly, is already specified after Eq. (8) in the "Results" section. For the sake of presenting an explicit models here and a better demonstration of the numerical results of Seifert surfaces in Fig. 2e, f of the main text, we adopt a slightly different construction here. We first define a function $f(k_w)$ as

$$f(k_w) = \prod_{n=1}^{M} \sin(k_w - \alpha_n),$$
(19)

where α_n is chosen as $0 < \alpha_n < \pi$, $\alpha_n \neq \pi/2$, and $\alpha_i \neq \alpha_j$ for $i \neq j$. This function has zeros at $k_{w,n} = \alpha_n$ and $k_{w,(M+n)} = \alpha_n + \pi$, with in total $2M$ different solutions to $f(k_w) = 0$. We next consider the following explicit $g_n(k_w)$,

$$g_n(k_w) = (\cos k_w + \cos k_{w,n}) \prod_{n' \neq n, n' \neq n-M}^{M} \sin(k_w - \alpha_{n'}),$$
(20)

which equals to zero at any $k_w = k_{w,m}$ except for $m = n$. Thus the total Hamiltonian

$$h_{N,4D}(\mathbf{k}) = \sum_{n=1}^{2M} h_{n,3D}(\mathbf{k}_{3D}) g_n(k_w) + f(k_w)\sigma_c$$
(21)

can host up to $2M$ NLs. To have $N \leq 2M$ NLs in this system, we let each $h_{n,3D}(\mathbf{k}_{3D})$ describe a 3D single-NL system for $n \in [1, N]$, and a 3D insulating system for $N < n \leq 2M$. For those with a 3D single-NL, $h_{n,3D}(\mathbf{k}_{3D})$ needs to satisfy certain symmetry to protect the NLs, e.g., the $P * T$ symmetry of $PT h_{n,3D}^*(\mathbf{k}_{3D})(PT)^{-1} = h_{n,3D}(\mathbf{k}_{3D})$, with PT a unitary operator. For simplicity, here we choose $h_{n,3D}(\mathbf{k}_{3D}) = \sigma_a + \sigma_b$ for all $N < n \leq 2M$. Therefore the system $h_{N,4D}(\mathbf{k})$ constructed above has N NLs, each given by a $h_{n,3D}(\mathbf{k}_{3D})$ at $k_w = k_{w,n}$ with $n \leq N$.

The above construction leads to the two specific examples in Fig. 2e, f. The first example is the Hopf-link, which is obtained by choosing $M = 1$ and $\alpha_1 = 0$. The Hamiltonian is given by

$$h_{4D}(\mathbf{k}) = h_{1,3D}(\mathbf{k}_{3D})(\cos k_w + 1) + h_{2,3D}(\mathbf{k}_{3D})(\cos k_w - 1) + (\sin k_w)\sigma_c, \quad (22)$$

with

$$h_{1,3D}(\mathbf{k}_{3D}) = [m - \cos(k_x + \alpha) - \cos k_y - \cos k_z]\sigma_a + (\sin k_y)\sigma_b;$$

$$h_{2,3D}(\mathbf{k}_{3D}) = -[m - \cos(k_x - \alpha) - \cos k_y - \cos k_z]\sigma_a - (\sin k_z)\sigma_b.$$

For $1 < m < 3$ and $\alpha = 0$, $h_{1,3D}(\mathbf{k}_{3D})$ and $h_{2,3D}(\mathbf{k}_{3D})$ give two NLs both centering at $(k_x, k_y, k_z) = (0, 0, 0)$. A nonzero α shifts the two NLs along k_x in opposite directions. When OBC is taken along the $\hat{w}$ direction, we obtain a pair of Hopf-link NLs in the 3D parameter space of $\mathbf{k}_{3D}$, and the boundary Fermi (zero-energy) surface gives the Seifert surface of the Hopf-link, as shown in Fig. 2e with $m = 2$ and $\alpha = \pi/4$.

The second example is a set of Borromean rings, which are three NLs linked together but any two of them are not linked. This is obtained by choosing $M = 2$, $\alpha_1 = 0$, $\alpha_2 = \pi/4$, with

$$h_{1,3D}(\mathbf{k}_{3D}) = (m - \cos k_x - B\cos k_y - A\cos k_z)\sigma_a + \sin k_x \sigma_b;$$

$$h_{2,3D}(\mathbf{k}_{3D}) = -(m - A\cos k_x - \cos k_y - B\cos k_z)\sigma_a - \sin k_y \sigma_b;$$

$$h_{3,3D}(\mathbf{k}_{3D}) = (m - B\cos k_x - A\cos k_y - \cos k_z)\sigma_a + \sin k_z \sigma_b,$$

and $h_{4,3D}^a = h_{4,3D}^b = 1$. The 4D Hamiltonian is then given by

$$\begin{aligned} h_{4D}(\mathbf{k}) = &\, h_{1,3D}(\mathbf{k}_{3D})(\cos k_w + 1)\sin(k_w - \pi/4) + h_{2,3D}(\mathbf{k}_{3D})(\cos k_w + \sqrt{2}/2)\sin k_w \\ &+ h_{3,3D}(\mathbf{k}_{3D})(\cos k_w - 1)\sin(k_w - \pi/4) + h_{4,3D}(\mathbf{k}_{3D})(\cos k_w - \sqrt{2}/2)\sin k_w \\ &+ \sin k_w \sin(k_w - \pi/4)\sigma_c. \end{aligned}$$
(23)

The coefficients A and B are to stretch the loops in different directions. Figure 2f of the main text has shown the Borromean rings and the boundary Fermi states with $m = 2$, $A = 1.2$ and $B = 0.6$.

Details of 2-link circuit and general circuit construction. In Fig. 4 we provide the lattice structure of the 2-link circuit in our simulation, whose spectrum relevant to the impedance is determined by the circuit Laplacian instead of the Hamiltonian. The real-space form of the circuit Laplacian, which determines the specific circuit components used, can be obtained from an inverse Fourier transformation

of ($J_{4D}(\mathbf{k})$ for Eq. (9)), which takes the following lattice form

$$
\begin{aligned}
-iJ_{4D} = &\sum_n 2m(\hat{a}^\dagger_{\uparrow,n}\hat{b}_{\downarrow,n} - \hat{a}^\dagger_{\downarrow,n}\hat{b}_{\uparrow,n}) + h.c. \\
&- \sum_n \frac{1}{2}\left[\hat{a}^\dagger_{\uparrow,n}\hat{b}_{\uparrow,n+\hat{w}} - \hat{a}^\dagger_{\uparrow,n}\hat{b}_{\uparrow,n-\hat{w}} - \hat{a}^\dagger_{\downarrow,n}\hat{b}_{\downarrow,n+\hat{w}} + \hat{a}^\dagger_{\downarrow,n}\hat{b}_{\downarrow,n-\hat{w}}\right] + h.c. \\
&+ \sum_n \left[-\frac{1}{2}\hat{a}^\dagger_{\uparrow,n}\hat{b}_{\downarrow,n+\hat{y}} - \frac{3}{2}\hat{a}^\dagger_{\uparrow,n}\hat{b}_{\downarrow,n-\hat{y}} + \frac{3}{2}\hat{a}^\dagger_{\downarrow,n}\hat{b}_{\uparrow,n+\hat{y}} + \frac{1}{2}\hat{a}^\dagger_{\downarrow,n}\hat{b}_{\uparrow,n-\hat{y}}\right] + h.c. \\
&+ \sum_n \left[-\frac{1}{2}\hat{a}^\dagger_{\uparrow,n}\hat{b}_{\downarrow,n+\hat{z}} - \frac{3}{2}\hat{a}^\dagger_{\uparrow,n}\hat{b}_{\downarrow,n-\hat{z}} + \frac{3}{2}\hat{a}^\dagger_{\downarrow,n}\hat{b}_{\uparrow,n+\hat{z}} + \frac{1}{2}\hat{a}^\dagger_{\downarrow,n}\hat{b}_{\uparrow,n-\hat{z}}\right] + h.c. \\
&+ \sum_n \frac{1}{2}\left[\hat{a}^\dagger_{\uparrow,n}\hat{b}_{\uparrow,n+\hat{x}+\hat{w}} + \hat{a}^\dagger_{\uparrow,n}\hat{b}_{\uparrow,n+\hat{x}-\hat{w}} + \hat{a}^\dagger_{\uparrow,n}\hat{b}_{\downarrow,n-\hat{x}+\hat{w}} + \hat{a}^\dagger_{\uparrow,n}\hat{b}_{\downarrow,n-\hat{x}-\hat{w}}\right] + h.c. \\
&- \sum_n \frac{1}{2}\left[\hat{a}^\dagger_{\downarrow,n}\hat{b}_{\downarrow,n+\hat{x}+\hat{w}} + \hat{a}^\dagger_{\downarrow,n}\hat{b}_{\uparrow,n+\hat{x}-\hat{w}} + \hat{a}^\dagger_{\downarrow,n}\hat{b}_{\uparrow,n-\hat{x}+\hat{w}} + \hat{a}^\dagger_{\downarrow,n}\hat{b}_{\downarrow,n-\hat{x}-\hat{w}}\right] + h.c. \\
&- \sum_n \frac{1}{4}\left[\hat{a}^\dagger_{\uparrow,n}\hat{b}_{\downarrow,n+\hat{y}+\hat{w}} + \hat{a}^\dagger_{\uparrow,n}\hat{b}_{\downarrow,n+\hat{y}-\hat{w}} - \hat{a}^\dagger_{\uparrow,n}\hat{b}_{\downarrow,n-\hat{y}+\hat{w}} - \hat{a}^\dagger_{\uparrow,n}\hat{b}_{\downarrow,n-\hat{y}-\hat{w}}\right] + h.c. \\
&- \sum_n \frac{1}{4}\left[\hat{a}^\dagger_{\downarrow,n}\hat{b}_{\uparrow,n+\hat{y}+\hat{w}} + \hat{a}^\dagger_{\downarrow,n}\hat{b}_{\uparrow,n+\hat{y}-\hat{w}} - \hat{a}^\dagger_{\downarrow,n}\hat{b}_{\uparrow,n-\hat{y}+\hat{w}} - \hat{a}^\dagger_{\downarrow,n}\hat{b}_{\uparrow,n-\hat{y}-\hat{w}}\right] + h.c. \\
&+ \sum_n \frac{1}{4}\left[\hat{a}^\dagger_{\uparrow,n}\hat{b}_{\downarrow,n+\hat{z}+\hat{w}} + \hat{a}^\dagger_{\uparrow,n}\hat{b}_{\downarrow,n+\hat{z}-\hat{w}} - \hat{a}^\dagger_{\uparrow,n}\hat{b}_{\downarrow,n-\hat{z}+\hat{w}} - \hat{a}^\dagger_{\uparrow,n}\hat{b}_{\downarrow,n-\hat{z}-\hat{w}}\right] + h.c. \\
&+ \sum_n \frac{1}{4}\left[\hat{a}^\dagger_{\downarrow,n}\hat{b}_{\uparrow,n+\hat{z}+\hat{w}} + \hat{a}^\dagger_{\downarrow,n}\hat{b}_{\uparrow,n+\hat{z}-\hat{w}} - \hat{a}^\dagger_{\downarrow,n}\hat{b}_{\uparrow,n-\hat{z}+\hat{w}} - \hat{a}^\dagger_{\downarrow,n}\hat{b}_{\uparrow,n-\hat{z}-\hat{w}}\right] + h.c.
\end{aligned}
\tag{24}
$$

As mentioned in the main text, each capacitor or inductor contributes a $i\omega C$ or $(i\omega L)^{-1}$ term to the Laplacian. In the above, they respectively contribute a ωC and $-1/(\omega L)$ term to $-iJ_{4D}$, with the effect of their effective resistivities leading to non-Hermitian contributions that are treated in the Supplementary Note 3. As such, positive and negative couplings can be implemented by capacitors and inductors respectively. To realize Eq. (24), capacitors with capacitance ratios matching that of the positive coefficients of Eq. (24), i.e., 1/4:1/2:3/2 etc. are first chosen. Next, inductors are also similarly chosen such that they reproduce the (inverse) ratios of the negative coefficients $-1/4, -1/2, -3/2$ etc. The combined choices of the capacitors and inductors determine the AC frequency ω at which the circuit should be driven: Suppose the $\pm 1/2$ coefficients are implemented by components C' and L'. Then the appropriate ω can be determined by requiring that the ratio of their admittances $|i\omega C'/(i\omega L')^{-1}| = \omega^2 L'C'$ is unity, i.e., $\omega = \frac{1}{\sqrt{LC}}$. If the AC frequency were to be varied from this value, the Laplacian will no longer correctly reproduce the desired tight-binding model Eq. (24), and the Seifert surface will slowly disappear as it becomes increasingly away from topolectrical resonance[54]. To partially counteract this, additional grounding capacitors or inductors can also be introduced to provide a tunable "chemical potential" that shifts the resonance in admittance space[54], as explored in additional simulations in the Supplementary Note 3. This requirement for an appropriate AC frequency in obtaining a desired circuit Laplacian pertains to all topolectrical circuit setups, and is very easily satisfied since standard signal generators operate over a wide range of frequencies.

Note that in Eq. (24) we have neglected the total conductance of each node, which contributes some diagonal terms to the Laplacian. In the particular circuit described of Fig. 5, this term shall be given by $h_d\sigma_3\tau_3$ with $h_d = 2m - 2$, while the rest of the Laplacian takes the form of $[\mathbf{h}(\mathbf{k})\cdot\boldsymbol{\sigma}]\tau_2$ in momentum space. This diagonal term will enlarge the NLs into nodal tori, as the zero condition is changed from $h_1 = h_2 = 0$ to $h_1^2 + h_2^2 = h_d^2$. These tori may merge into each other when the diagonal term is large, and hence change the knot structure and the Seifert surface. In a more general scenario, additional diagonal terms may also gap out the Seifert surface, e.g., a $\sigma_0\tau_3$ term added to our system. Nevertheless, these diagonal modification can be easily counteracted by adding an unequal amount of grounding capacitors or inductors to each sublattice[54]. In our specific setup, the diagonal term of h_d does not need to be perfectly counteracted, as long as the amount is small enough to avoid merging of the NLs (tori).

Since Eq. (24) is a 4-band model, the circuit lattice consists of 4-node unit cells. This, together with their LC connections, is illustrated in Fig. 4a, b. As previously highlighted, although we are working with a 4D circuit lattice, the circuit connections can be spatially arranged such that it is essentially defined on a 3D lattice with more complicated nodes and connections (Fig. 4a). The construction of other nodal structures is exactly analogous.

Practically, the circuit may be constructed in a modular manner, with individual subunits tested such that necessary idiosyncrasies in their physical embedding (convoluted or looping wires) do not lead to uneven resistivities or unwanted mutual inductances. To minimize such effects, high quality shielded copper wires may be required for some connections, as well and metal foils can be helpful for isolating the inductors. It is also imperative to strictly filter and select the components used, such that their disorder within manufacturer specifications can be further minimized. Exploiting the scale-invariant nature of our 4D circuit model, the actual circuit can be built as large as possible such that irregularities can be easily debugged by hand.

When $1 < m < 3$, $h_{1,3D}(\mathbf{k}_{3D})$ from Eq. (10) gives a NL in $k_x - k_z$ plane, centering at $\mathbf{k}_{3D} = (0, 0, 0)$; and $h_{2,3D}(\mathbf{k}_{3D})$ from Eq. (11) gives another NL in $k_x - k_y$ plane, centering at $\mathbf{k}_{3D} = (\pi, 0, 0)$. These two loops are linked to each other when $1 < m < 2$, as shown in Fig. 4c with $m = 1.5$. In a local region near the momentum where the two loops are linked [e.g., $0 < k_x < \pi$ in Fig. 4c], the Seifert surface resembles that of a Hopf link, which consists of two loops with one mutual nodal linkage, and a Seifert surface that locally resembles a "soap bubble" terminating on the edges of two interlocking rings. The energy dispersion of this model is given by

$$
E = \pm\sqrt{P_1^2 + Q_1^2 + \sin^2 k_w},
\tag{25}
$$

with $P_1 = (\sin k_y - \sin k_z)\cos k_w - (\sin k_y + \sin k_z)$ and $Q_1 = 2(\cos k_y + \cos k_z - m) - 2\cos k_x \cos k_w$. This Hamiltonian describes a 4-band model with two-fold degeneracy, and its energy dispersion is identical to the one of an analytically simpler 2-band model, described by Eq. (24) of the main text without the τ_2. However, here we have to form a tensor product with τ_2 in order to have back the time-reversal symmetry, which reads

$$
J^*(\mathbf{k}) = -J(-\mathbf{k})
\tag{26}
$$

as the Laplacian resembles a spinless Hamiltonian with $J \to iH$.

Due to the topologically non-trivial 3-torus BZ where this 2-link is embedded in, the latter becomes trivially linked, even though it is locally similar to the non-trivially linked Hopf-link. Nevertheless, the Seifert surface which interpolates the two NLs is highly non-trival, having a similar structure as that of a Hopf-link (Fig. 2e) locally near linkages, but stretching across the two NLs in a different way. This is reflected in the non-trivial form of its Seifert matrix, which contains more information than its Alexander polynomial which vanishes due to its trivial NL linkages (Table 1).

Details of the Trefoil knot circuit. The Trefoil knot circuit used in the simulation presented in Fig. 5b is more complicated, and we shall just present its momentum-space structure. It can be numerically verified that $h_{3D}(\mathbf{k}_{3D}) = h_1(\mathbf{k}_{3D})\sigma_1 + h_3(\mathbf{k}_{3D})\sigma_3$ gives, via Eqs. (3) to (5), an optimized RLC nodal Trefoil knot circuit with

$$
\begin{aligned}
h_1(\mathbf{k}_{3D}) = &-6\cos k_x\cos k_y\cos 2k_z - 0.6\cos k_x\cos k_y - 3\cos^2 k_x\cos 2k_z + 12\cos k_x\cos 2k_z - 6\cos k_x\cos k_z\cos 2k_z \\
&- 0.6\cos k_x\cos k_z - \sin^2 k_x + 1.2\cos k_x - 3\cos^2 k_y\cos 2k_z + 12\cos k_y\cos 2k_z - 6\cos k_y\cos k_z\cos 2k_z \\
&- 0.6\cos k_y\cos k_z + \sin^2 k_z + 1.2\cos k_y + \cos^3 k_z + 0.3\cos^2 2k_z - 3\cos^2 k_z\cos 2k_z + 12\cos k_z\cos 2k_z \\
&- 12\cos 2k_z + 1.2\cos k_z - 1.2,
\end{aligned}
\tag{27}
$$

$$
\begin{aligned}
h_3(\mathbf{k}_{3D}) = &-6\cos k_x\cos k_y\cos k_z - 2\sin k_x\sin k_y - 3\cos^2 k_x\cos k_y - 3\cos k_x\cos^2 k_y + 12\cos k_x\cos k_y \\
&- 3\cos^2 k_x\cos k_z - 3\cos k_x\cos^2 k_z + 3\cos k_x\cos^2 2k_z + 12\cos k_x\cos k_z + 0.6\cos k_x\cos 2k_z \\
&- \cos^3 k_x + 6\cos^2 k_x - 11.97\cos k_x - 3\cos k_y\cos^2 k_z + 3\cos k_y\cos^2 2k_z + 3\cos^2 k_y\cos 2k_z \\
&+ 12\cos k_y\cos k_z + 0.6\cos k_y\cos 2k_z - \cos^3 k_y + 6\cos^2 k_y - 11.97\cos k_y - \cos^3 k_z + 6\cos^2 k_z \\
&+ 3\cos k_z\cos^2 2k_z - 6\cos^2 2k_z - 11.97\cos k_z + 0.6\cos k_z\cos 2k_z - 1.2\cos 2k_z + 7.94.
\end{aligned}
\tag{28}
$$

Perturbations away from these values do not change the topology unless they are sufficiently large.

Data availability
The data that support the plots within this paper and other findings of this study are available from any of the authors upon reasonable request.

Code availability
Though not essential to the central conclusions of this work, computer codes used to generate Figs. 3(d–f) and 5 in the main text, and Supplementary Figs. 3–9 are available upon reasonable request via email to C.H.L.

References
1. Javier, A., Vázquez, M., Trigueros, S. & Roca, J. Knotting probability of DNA molecules confined in restricted volumes: DNA knotting in phage capsids. *Proc. Natl Acad. Sci. USA* **99**, 5373–5377 (2002).
2. Moore, N. T., Lua, R. C. & Grosberg, A. Y. Topologically driven swelling of a polymer loop. *Proc. Natl Acad. Sci. USA* **101**, 13431–13435 (2004).
3. Larocque, H. et al. Reconstructing the topology of optical polarization knots. *Nat. Phys.* **14**, 1079 (2018).
4. Zhong, C. et al. Three-dimensional Pentagon Carbon with a genesis of emergent fermions. *Nat. Commun.* **8**, 15641 (2017).
5. Ezawa, M. Topological semimetals carrying arbitrary Hopf numbers: Fermi surface topologies of a Hopf link, Solomon's knot, trefoil knot, and other linked nodal varieties. *Phys. Rev. B* **96**, 041202 (2017).

6. Yan, Z. et al. Nodal-link semimetals. *Phys. Rev. B* **96**, 041103 (2017).
7. Chen, W., Lu, H.-Z. & Hou, J.-M. Topological semimetals with a double-helix nodal link. *Phys. Rev. B* **96**, 041102 (2017).
8. Li, L., Chesi, S., Yin, C. & Chen, S. 2π-flux loop semimetals. *Phys. Rev. B* **96**, 081116 (2017).
9. Sun, X.-Q., Lian, B. & Zhang, S.-C. Double Helix Nodal Line Superconductor. *Phys. Rev. Lett.* **119**, 147001 (2017).
10. Chang, G. et al. Topological Hopf and Chain Link Semimetal States and Their Application to Co_2MnGa. *Phys. Rev. Lett.* **119**, 156401 (2017).
11. Li, L., Lee, C. H. & Gong, J. Realistic Floquet semimetal with exotic topological linkages between arbitrarily many nodal loops. *Phys. Rev. Lett.* **121**, 036401 (2018).
12. Lee, C. H. et al. Imaging nodal knots in momentum space through topolectrical circuits. Preprint at https://arxiv.org/abs/1904.10183.
13. Stålhammar, M., Rødland, L., Arone, G., Budich, J. C.& Bergholtz, E. J. Hyperbolic nodal band structures and knot invariants. Preprint at https://arxiv.org/abs/1905.05858 https://doi.org/10.21468/SciPostPhys.7.2.019.
14. Lee, C. H. et al. Enhanced higher harmonic generation from nodal topology. Preprint at https://arxiv.org/abs/1906.11806.
15. Murasugi, K. *Knot Theory and its Applications* (Springer Science & Business Media, Berlin, 2007).
16. Collins, J. An algorithm for computing the Seifert matrix of a link from a braid representation. *ENSAIOS MATEMÁTICOS* **30**, 246 (2016).
17. Hasan, M. Z. & Kane, C. L. Colloquium: topological insulators. *Rev. Mod. Phys.* **82**, 3045 (2010).
18. Qi, X.-L. & Zhang, S.-C. Topological insulators and superconductors. *Rev. Mod. Phys.* **83**, 1057 (2011).
19. Burkov, A. A., Hook, M. D. & Balents, L. Topological nodal semimetals. *Phys. Rev. B* **84**, 235126 (2011).
20. Weng, H. et al. Topological node-line semimetal in three-dimensional graphene networks. *Phys. Rev. B* **92**, 045108 (2015).
21. Kim, Y., Wieder, B. J., Kane, C. L. & Rappe, A. M. Dirac line nodes in inversion-symmetric crystals. *Phys. Rev. Lett.* **115**, 036806 (2015).
22. Yu, R., Weng, H., Fang, Z., Dai, X. & Hu, X. Topological node-line semimetal and Dirac semimetal state in antiperovskite Cu_3PdN. *Phys. Rev. Lett.* **115**, 036807 (2015).
23. Ahn, J., Kim, D., Kim, Y. & Yang, B.-J. Band topology and linking structure of nodal line semimetals with Z_2 monopole charges. *Phys. Rev. Lett.* **121**, 106403 (2018).
24. Wang, Z., Wieder, B. J., Li, J., Yan, B. & Bernevig, B. A. Higher-Order Topology, Monopole Nodal Lines, and the Origin of Large Fermi Arcs in Transition Metal Dichalcogenides XTe_2 (X=Mo,W). Preprint at https://arxiv.org/abs/1806.11116.
25. Kirby, R. Problems in low-dimensional topology. *Proceedings of Georgia Topology Conference, Part 2* (1995).
26. Vafaee, F. Seifert surfaces distinguished by sutured Floer homology but not its Euler characteristic. *Topol. Appl.* **184**, 72 (2015).
27. van Wijk, J. J. & Cohen, A. M. Visualization of Seifert surfaces. *IEEE Transactions Visualization Computer Graphics* **12**, 485 (2006).
28. van Garderen, M. & van Wijk, J. J. Seifert surfaces with minimal genus. *Proceedings of Bridges 2013: Mathematics, Music, Art, Architecture, Culture.* 453–456 (Tessellations Publishing, 2013).
29. Carlström, J. & Bergholtz, E. J. Exceptional Links and Twisted Fermi Ribbons in non-Hermitian Systems. *Phys. Rev. A* **98**, 042114 (2018).
30. Carlström, J., Stålhammar, M., Budich, J. C. & Bergholtz, E. J. Knotted non-Hermitian metals. *Phys. Rev. B* **99**, 161115 (2019).
31. Yang, Z. & Hu, J. Nodal line semimetals under non-Hermitian perturbations-emerging Hopf-link exceptional line semimetals. *Phys. Rev. B* **99**, 081102 (2019).
32. Wang, H., Ruan, J. & Zhang, H. Non-Hermitian nodal-line semimetals. *Phys. Rev. B* **99**, 075130 (2019).
33. Moors, K., Zyuzin, A. A., Zyuzin, A. Y., Tiwari, R. P. & Schmidt, T. L. Disorder-driven exceptional lines and Fermi ribbons in tilted nodal-line semimetals. *Phys. Rev. B* **99**, 041116 (2019).
34. Luo, K., Feng, J., Zhao, Y. X. & Yu, R. Nodal manifolds bounded by exceptional points on non-Hermitian honeycomb lattices and electrical-circuit realizations. Preprint at https://arxiv.org/abs/1810.09231.
35. Bian, G. et al. Topological nodal-line fermions in spin-orbit metal $PbTaSe_2$. *Nat. Commun.* **7**, 10556 (2016).
36. Schoop, L. M. et al. Dirac cone protected by non-symmorphic symmetry and three-dimensional Dirac line node in ZrSiS Nat. *Commun.* **7**, 11696 (2016).
37. Takane, D. et al. Dirac-node arc in the topological line-node semimetal HfSiS. *Phys. Rev. B* **94**, 121108 (2016).
38. Chen, C. et al. Dirac line nodes and effect of spin-orbit coupling in the nonsymmorphic critical semimetals MSiS (M = Hf, Zr). *Phys. Rev. B* **95**, 125126 (2017).
39. Deng, W. et al. Nodal rings and drumhead surface states in phononic crystals. *Nat. Commun.* **10**, 1769 (2019).
40. Hosen, M. M. et al. Observation of topological nodal-loop state in RAs_3 (R = Ca, Sr). Preprint at https://arxiv.org/abs/1812.06365.
41. Kraus, Y. E., Ringel, Z. & Zilberberg, O. Four-dimensional Quantum Hall Effect in a two-dimensional quasicrystal. *Phys. Rev. Lett.* **111**, 226401 (2013).
42. Price, H. M., Zilberberg, O., Ozawa, T., Carusotto, I. & Dolgman, N. Four-deminsional quantum Hall effect with ultracold atoms. *Phys. Rev. Lett.* **115**, 195303 (2015).
43. Lohse, M., Schweizer, C., Price, H. M., Zilberberg, O. & Bloch, I. Exploring 4D quantum Hall physics with a 2D topological charge pump. *Nature* **553**, 53 (2018).
44. Zilberberg, O. et al. Photonic topological boundary pumping as a probe of 4D quantum Hall physics. *Nature* **553**, 59 (2018).
45. Zhang, S.-C. & Hu, J. A four-dimensional generalization of the Quantum Hall Effect. *Science* **294**, 823 (2001).
46. Qi, X.-L., Hughes, T. L. & Zhang, S.-C. Topological field theory of time-reversal invariant insulators. *Phys. Rev. B* **78**, 195424 (2008).
47. Lian, B. & Zhang, S.-C. Five-dimensional generalization of the topological Weyl semimetal. *Phys. Rev. B* **94**, 041105 (2016).
48. Lian, B. & Zhang, S.-C. Weyl semimetal and topological phase transition in five dimensions. *Phys. Rev. B* **95**, 235106 (2017).
49. Altland, A. & Zirnbauer, M. R. Nonstandard symmetry classes in mesoscopic normal-superconducting hybrid structures. *Phys. Rev. B* **55**, 1142 (1997).
50. Schnyder, A. P., Ryu, S., Furusaki, A. & Ludwig, A. W. W. Classification of topological insulators and superconductors in three spatial dimensions. *Phys. Rev. B* **78**, 195125 (2008).
51. Kitaev, A. Periodic table for topological insulators and superconductors. *AIP Conf. Proc.* **1134**, 22 (2009).
52. Albert, V. V., Glazman, L. I. & Jiang, L. Topological properties of linear circuit lattices. *Phys. Rev. Lett.* **114**, 173902 (2015).
53. Ningyuan, J., Owens, C., Sommer, A., Schuster, D. & Simon, J. Time-and site-resolved dynamics in a topological circuit. *Phys. Rev. X* **5**, 021031 (2015).
54. Lee, C. H. et al. Topolectrical circuits. *Communications Physics* **1**, 39 (2018).
55. Imhof, S. et al. Topolectrical circuit realization of topological corner modes. *Nature Physics* **14**, 925 (2018).
56. Lu, Y. et al. Probing the Berry curvature and Fermi arcs of a Weyl circuit. *Phys. Rev. B* **99**, 020302 (2019).
57. Luo, J., Yu, R. & Weng, H. Topological Nodal States in Circuit Lattice. *Research* **2018**, 6793752 (2018).
58. Hadad, Y., Soric, J. C., Khanikaev, A. B. & Al`u, A. Self-induced topological protection in nonlinear circuit arrays. *Nat. Electronics* **1**, 178 (2018).
59. Zhu, W., Hou, S., Long, Y., Chen, H. & Ren, J. Simulating quantum spin Hall effect in the topological Lieb lattice of a linear circuit network. *Phys. Rev. B* **97**, 075310 (2018).
60. Goren, T., Plekhanov, K., Appas, F. & Hur, K. L. Topological Zak phase in strongly coupled LC circuits. *Phys. Rev. B* **97**, 041106 (2018).
61. Helbig, T. et al. Band structure engineering and reconstruction in electric circuit networks. *Phys. Rev. B* **99**, 161114 (2019).
62. Hofmann, T., Helbig, T., Lee, C. H. & Thomale, R. Chiral voltage propagation and calibration in a topolectrical Chern circuit. *Phys. Rev. Lett.* **122**, 247702 (2019).
63. Wang, Y., Lang, L. J., Lee, C. H., Zhang, B. & Chong, Y. D. Topologically enhanced harmonic generation in a nonlinear transmission line metamaterial. *Nat. Commun.* **10**, 1102 (2019).
64. Yang, Y.-B., Duan, L.-M. & Xu, Y. Dynamical Weyl Points and 4D Nodal Rings in Cold Atomic Gases. *Phys. Rev. B* **98**, 165128 (2018).
65. Burkov, A. A. Quantum anomalies in nodal line semimetals. *Phys. Rev. B* **97**, 165104 (2018).
66. Lu, B., Yada, K., Sato, M. & Tanaka, Y. Crossed surface flat bands of Weyl semimetal superconductors. *Phys. Rev. Lett.* **114**, 096804 (2015).
67. Boada, O., Celi, A., Latorre, J. I. & Lewenstein, M. Quantum simulation of an extra dimension. *Phys. Rev. Lett.* **108**, 133001 (2012).
68. Celi, A. et al. Synthetic gauge fields in synthetic dimensions. *Phys. Rev. Lett.* **112**, 043001 (2014).
69. Mancini, M. et al. Observation of chiral edge states with neutral fermions in synthetic Hall ribbons. *Science* **349**, 1510 (2015).
70. Stuhl, B. K., Lu, H. I., Aycock, L. M., Genkina, D. & Spielman, I. B. Visualizing edge states with an atomic Bose gas in the quantum Hall regime. *Science* **349**, 1514 (2015).

Acknowledgements

Author contributions

J.G. initiated this project. L.L. conceived the idea of zero-energy boundary surfaces of 4D topological matter and proposed models. C.H.L. refined the project and worked out the circuit realizations and the topological classification. All authors discussed the theoretical and computational results and contributed to the writing of the manuscript.

Competing interests

The authors declare no competing interests.

Additional information

Supplementary information is available for this paper at https://doi.org/10.1038/s42005-019-0235-4.

Correspondence and requests for materials should be addressed to L.L., C.H.L. or J.G.

Reprints and permission information is available at http://www.nature.com/reprints

Publisher's note Springer Nature remains neutral with regard to jurisdictional claims in published maps and institutional affiliations.